Supporting Information

Synergy of Mechanical, Antifouling and Permeation Properties of Carbon Nanotube Nanohybrid Membrane for Efficient Oil/Water Separation

*Yanan Liu[a,c], Yanlei Su[a,c], Jialin Cao[a,c], Jingyuan Guan[a,c], Linyan Xu[b], Rannan Zhang[a,c], Mingrui He[a,c], Qi Zhang[a,c], Lin Fan[a,c], Zhongyi Jiang[a,c]**

a Key Laboratory for Green Chemical Technology of Ministry of Education, School of Chemical Engineering and Technology, Tianjin University, Tianjin 300072, China

b State Key Laboratory of Precision Measuring Technology and Instruments, Tianjin University, Tianjin 300072, China

c Collaborative Innovation Center of Chemical Science and Engineering (Tianjin), Tianjin 300072, China

∗ Corresponding author. School of Chemical Engineering and Technology, Tianjin University, No. 92, Weijin Road, Nankai District, Tianjin 300072, China

Tel: 86-22-27406646. Fax: 86-22-23500086.

E-mail address: zhyjiang@tju.edu.cn (Z.Y. Jiang)

1. The average pore size and SEM image of non-woven fabrics.

The SEM image of non-woven fabrics which was used as the support of the nPEI@CNT-m hybrid ultrafiltration membranes during oil/water separation process was shown in Fig. S1, and the average pore size was about 30 μm.

Fig. S1. SEM image of non-woven fabrics

2. The droplet size of the surfactant-stabilized oil-in-water emulsions.

The droplet size distribution of surfactant-stabilized oil-in-water emulsion including soybean oil-in-water, hexadecane-in-water and pump oil-in-water emulsion was examined by Zeta PALS, as shown in Fig. S2.

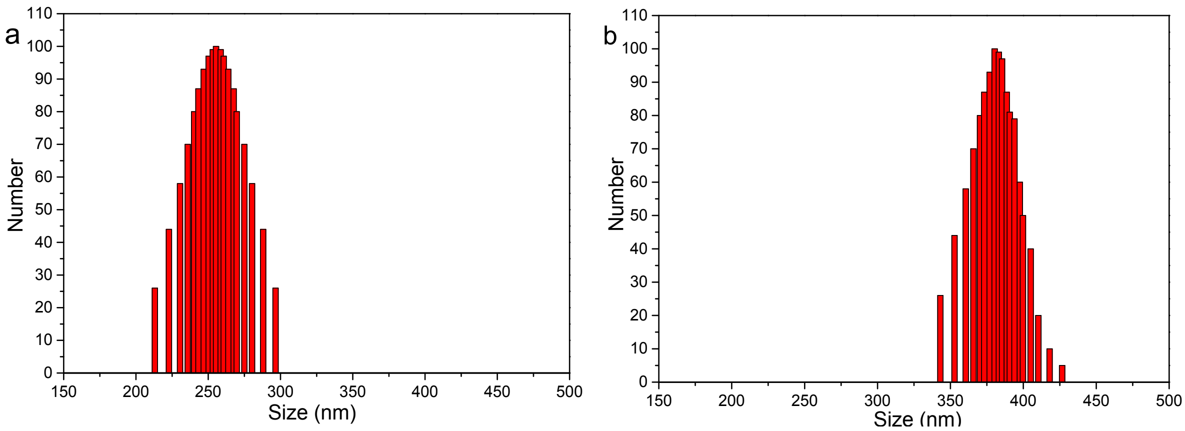

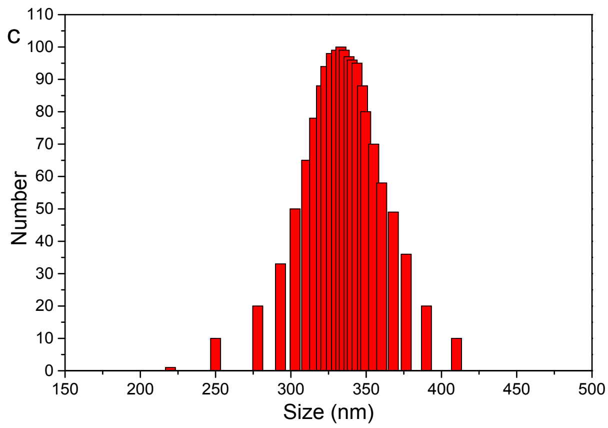

Fig. S2. The droplet size distribution of surfactant-stabilized oil-in-water emulsions (a) soybean oil-in-water (b) hexadecane-in-water (c) pump oil-in-water

3. TEM images of PEI_{10}@CNT, PEI_{15}@CNT and PEI_{20}@CNT dispersions

The TEM images of PEI_{10}@CNT, PEI_{15}@CNT and PEI_{20}@CNT dispersions showed that the PEI nanocoating on carbon nanotube was about 1.22 nm, 1.74 nm and 2.13 nm in thickness, respectively. And the thickness of PEI on CNTs increased as the mass ratio of PEI to CNTs increased.

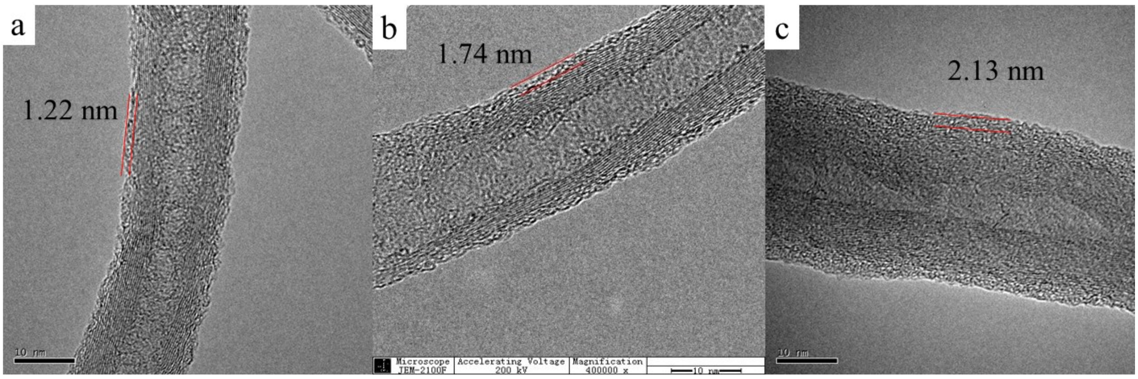

Fig. S3. TEM images of PEI_{10}@CNT, PEI_{15}@CNT and PEI_{20}@CNT dispersions.

4. The thermogravimetric analysis (TGA) measurement of PEI@CNT nanohybrid membranes

Thermogravimetric analysis (TGA) was used to determine the composition of the dried PEI@CNT nanohybrid membranes. Fig. S4 showed the TGA curves and decomposition temperature values of CNTs, PEI_{10}@CNT_{120}, PEI_{15}@CNT_{120} and PEI_{20}@CNT_{120}, and it could be found that PEI began to decompose at about 155°C and CNTs had no obvious decomposition in the temperature range of 50

^{o}C to 350 ^{o}C. Therefore, the percentages of PEI and the mass ratio of PEI to CNTs in the $PEI_x@CNT_y$ nanohybrid membranes could be obtained, as shown in Fig. S4. The percentages of PEI were 91.5%, 93.9% and 95.3% for $PEI_{10}@CNT_{120}$, $PEI_{15}@CNT_{120}$ and $PEI_{20}@CNT_{120}$. And the mass ratios of PEI to CNTs were 10.76, 15.39 and 20.27 for $PEI_{10}@CNT_{120}$, $PEI_{15}@CNT_{120}$ and $PEI_{20}@CNT_{120}$, which was identical to the original mass ratio of PEI to CNTs during the preparation process of PEI@CNT dispersions. Accordingly, the amount of PEI in the PEI@CNT nanohybrid membranes was determined.

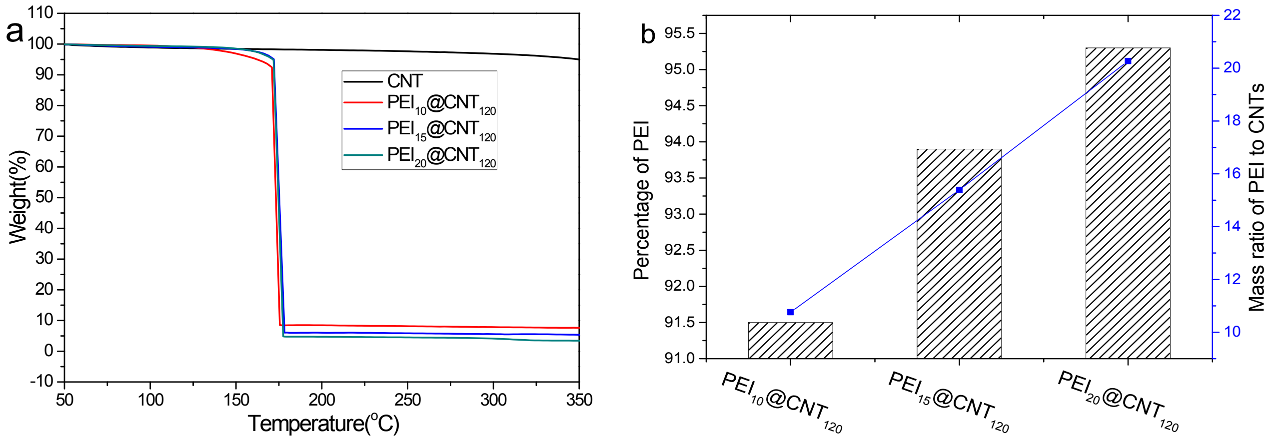

Fig. S4. (a) Thermogravimetric analysis of CNTs, $PEI_{10}@CNT_{120}$, $PEI_{15}@CNT_{120}$ and $PEI_{20}@CNT_{120}$ at temperature range of 50 ^{o}C to 350 ^{o}C. (b) Percentage of PEI and mass ratio of PEI to CNTs in $PEI_{10}@CNT_{120}$, $PEI_{15}@CNT_{120}$ and $PEI_{20}@CNT_{120}$.

5. The SEM and TEM images of PEI@CNT nanohybrid membranes

The mass ratio of PEI to CNTs affected the assembly of CNTs and led to different pore structure of membranes as shown in Fig. S5. And with the mass ratio of PEI to CNTs increased, the thickness of the membranes increased, as shown in the SEM images of cross-section, and the same conclusion was derived from TEM images.

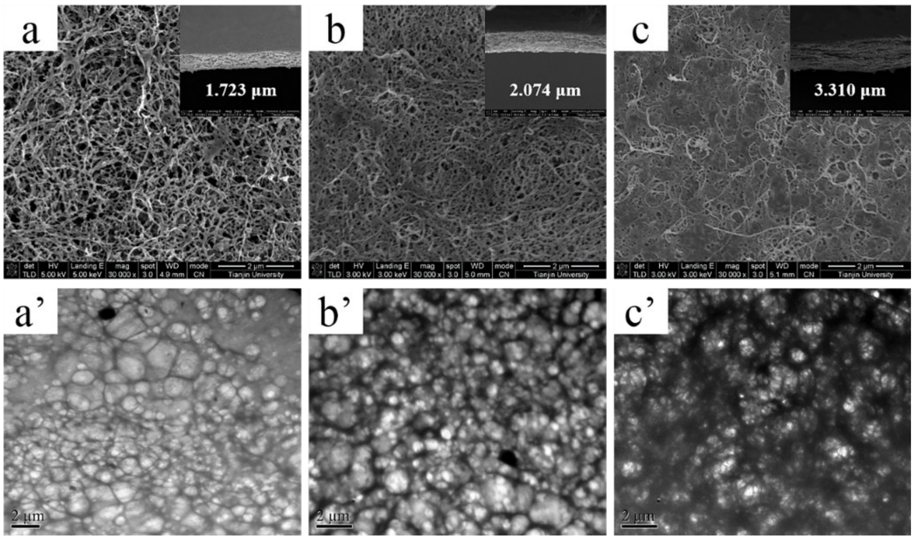

Fig. S5. SEM and TEM images of prepared membranes. (a, a') PEI_{10}@CNT_{120}, (b, b') PEI_{15}@CNT_{120}, (c, c') PEI_{20}@CNT_{120}. The insets are the SEM images of cross-section.

6. The AFM images of PEI@CNT nanohybrid membranes

AFM was used to measure the surface roughness of PEI@CNT nanohybrid membranes, as shown in Fig. S6. The PEI_{10}@CNT_{120} membrane contained lesser PEI, and there was obvious CNTs existing on the membrane surface, which could be derived from Fig. S5. Furthermore, more PEI used to modify CNTs would lead to lesser CNTs exposed on the membrane surface, and an excess of PEI would fill the network of CNTs resulting in smaller pore size and smoother surface. The surface roughness of PEI@CNT nanohybrid membranes decreased with the increase of PEI adding amount.

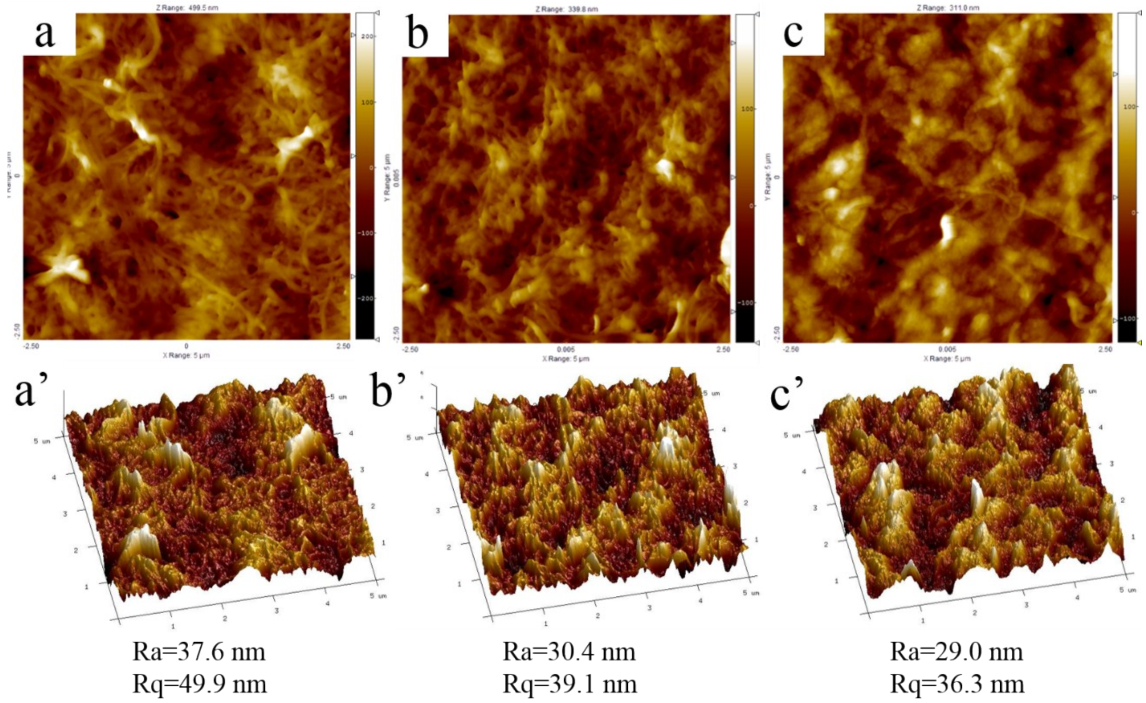

Fig. S6. AFM images of PEI@CNT nanohybrid membranes. (a, a') $PEI_{10}@CNT_{120}$, (b, b') $PEI_{15}@CNT_{120}$ and (c, c') $PEI_{20}@CNT_{120}$.

7. The average pore sizes, surface porosity and surface roughness parameters of $PEI_{10}@CNT_{120}$, $PEI_{15}@CNT_{120}$ and $PEI_{20}@CNT_{120}$.

The effective pore size and porosity of the PEI@CNT nanohybrid membranes decreased as the mass ratio of PEI to CNTs increased. The effective pore size of $PEI_{10}@CNT_{120}$, $PEI_{15}@CNT_{120}$ and $PEI_{20}@CNT_{120}$ were 141.9 nm, 73.5 nm and 40.0 nm, respectively, and the porosity of $PEI_{10}@CNT_{120}$, $PEI_{15}@CNT_{120}$ and $PEI_{20}@CNT_{120}$ were 58.6%, 36.6% and 17.2%, respectively

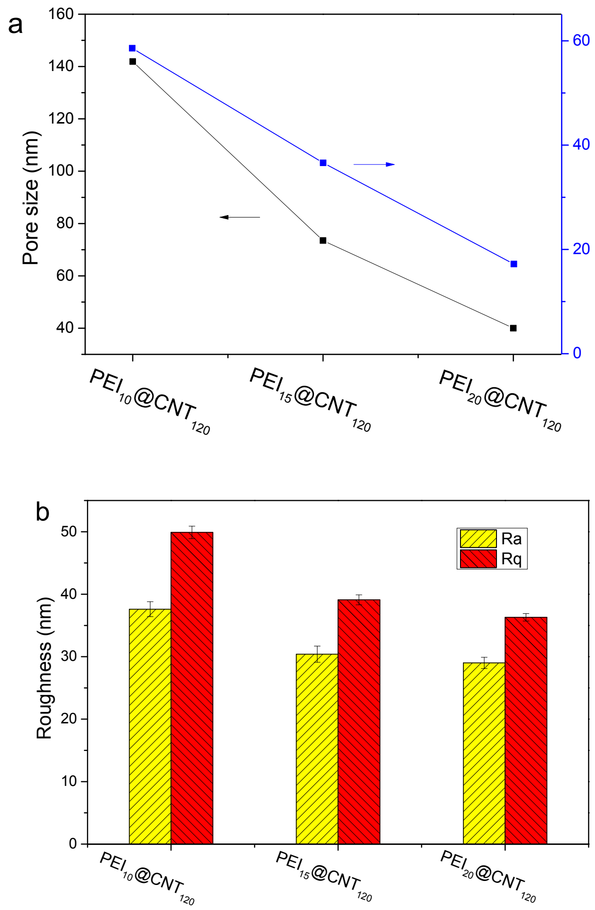

Fig. S7. (a) The average pore sizes and surface porosity of PEI_{10}@CNT_{120}, PEI_{15}@CNT_{120} and PEI_{20}@CNT_{120}. (b) The surface roughness of PEI_{10}@CNT_{120}, PEI_{15}@CNT_{120} and PEI_{20}@CNT_{120}

8. The pore size and porosity of the PEI_{15}@CNT_{120}, PEI_{15}@CNT_{120}-TMC_2 and PEI_{15}@CNT_{120}-TMC_5 nanohybrid membranes

Due to the modification of TMC, the pore size and porosity of the as-prepared membranes decreased, and with the immersing time increased, the pore size and porosity decreased.

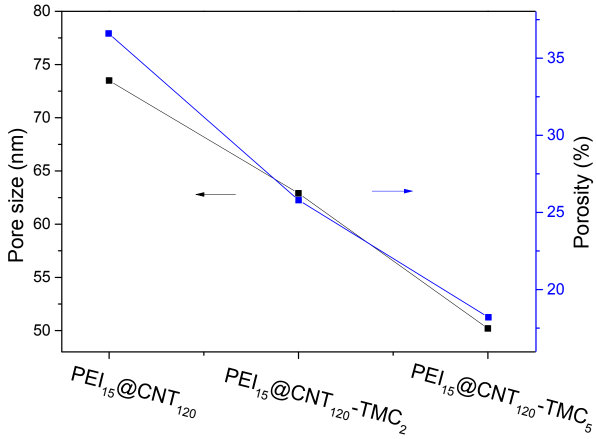

Fig. S8. The pore size and porosity of the $PEI_{15}@CNT_{120}$, $PEI_{15}@CNT_{120}$-TMC_2 and $PEI_{15}@CNT_{120}$-TMC_5 nanohybrid membranes

9. The Young's modulus of the membranes

The Young's modulus of the PEI@CNT and PEI@CNT-TMC nanohybrid membranes was measured by AFM with peak force tapping mode, as the mass ratio of PEI to CNT increased, the Young's modulus increased. Moreover, as immersing time in TMC heptane solution increased, the Young's modulus increased.

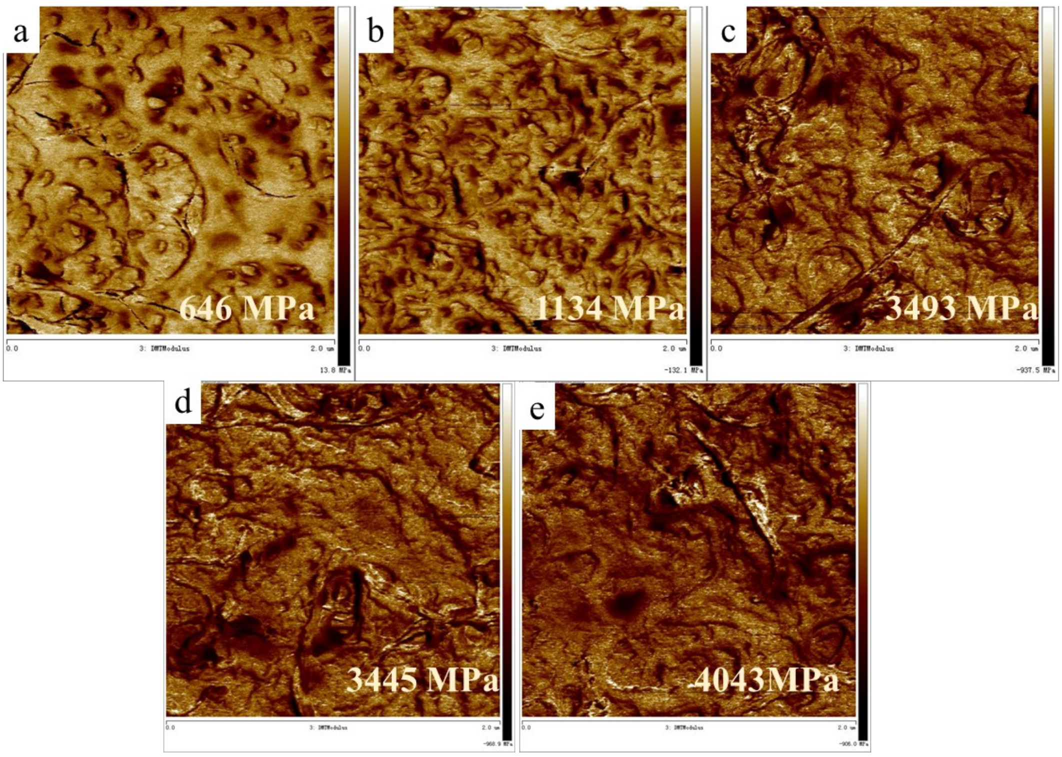

Fig. S9. The Young's modulus of (a) PEI_{10}@CNT_{120} (b) PE_{15}@CNT_{120}, (c) PEI_{20}@CNT_{120} (d) PEI_{15}@CNT_{120}-TMC_2 and (d) PEI_{15}@CNT_{120}-TMC_5.

10. The water contact angle of CNT film

Due to the hydrophobicity of CNT, the water contact angle of CNT film was about 110°, as shown in Fig. S10.

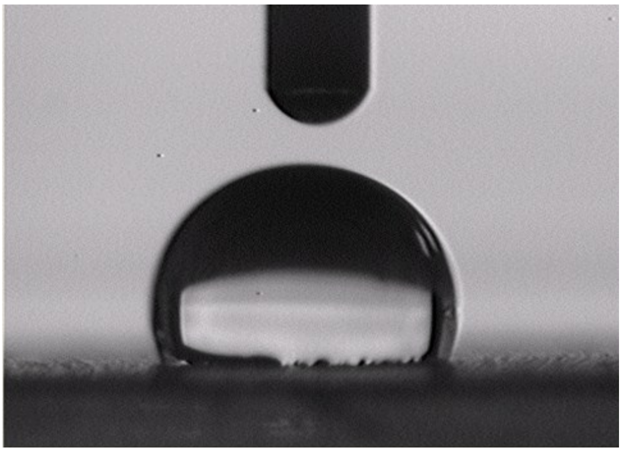

Fig. S10. The water contact angle of CNT film.

11. The photograph of AFM tip with oil droplet.

The hydrophobicity of AFM tip ensured the stable adsorption of oil droplet on the AFM tip during the measurement process. And the size of oil droplet was about 75 μm.

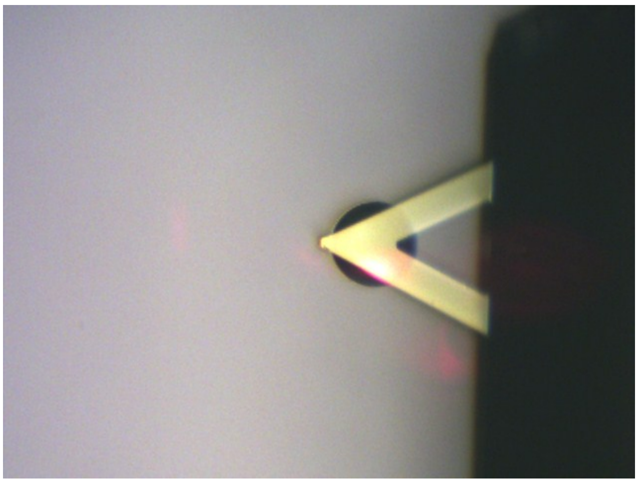

Fig. S11. The photograph of AFM tip with oil droplet.

12. The water contact angle, air contact angle underwater, oil contact angle underwater and

the dynamic measurements of oil-adhesion underwater of silicon wafer

The silicon wafer was commonly used hydrophilic material. The as-prepared membranes in this study possessed excellent hydrophilicity. For comparison, the wettability of silicon wafer was measured as shown in Fig. S12. The water contact angle of silicon wafer was 51°. However, the air contact angle and oil contact angle underwater were 133° and 121°, respectively. And the dynamic measurement of oil-adhesion underwater of silicon wafer demonstrated that the silicon wafer did not possess underwater super-oleophobicity, which was in good agreement with the interaction force measurement.

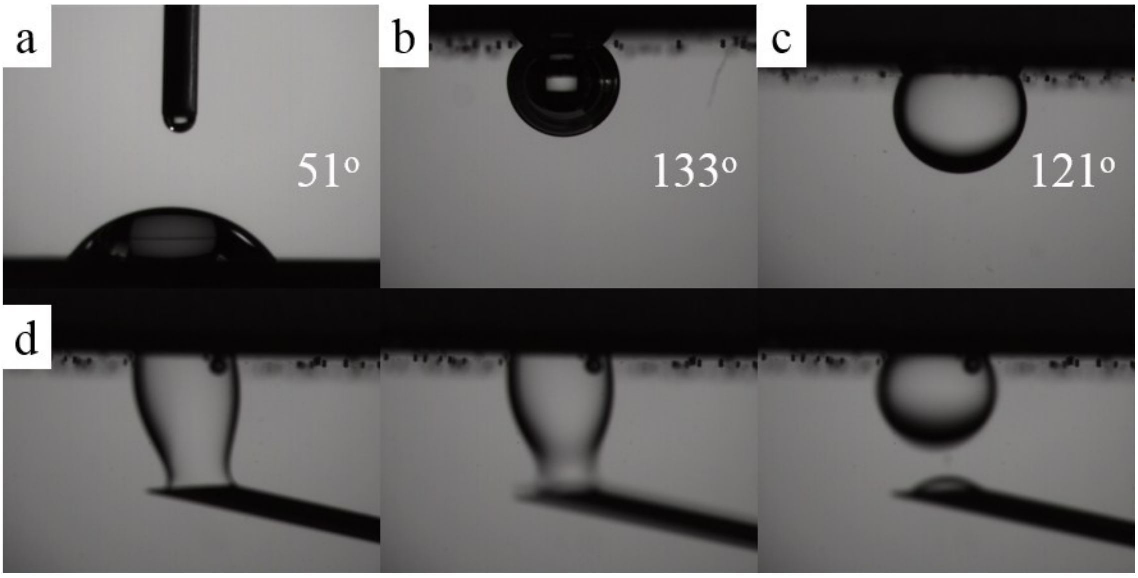

Fig. S12. (a) the water contact angle (b) the air contact angle underwater (c) the oil contact angle underwater of silicon wafer. (d) the dynamic measurements of oil-adhesion underwater of silicon wafer

13. The thickness and water permeation flux of the PEI@CNT nanohybrid membranes with different filtration volumes of the PEI@CNT dispersions and the mass ratio of PEI to CNTs.

As the mass ratio of PEI to CNTs increased, the surface porosity and pore size decreased, and the thickness increased. Accordingly, the flux decreased as the mass ratio of PEI to CNTs increased.

And when the volume of PEI@CNT dispersions increased, the thickness of the prepared membranes increased. Hence, the volume of PEI@CNT dispersions was inversely proportional to the flux. The PEI@CNT nanohybrid membranes possessed high water permeation flux reaching 9493 L m^{-2} h^{-1} bar^{-1} which was about 10 folds of the water permeation flux of the membrane made by non-solvent induced phase separation process.

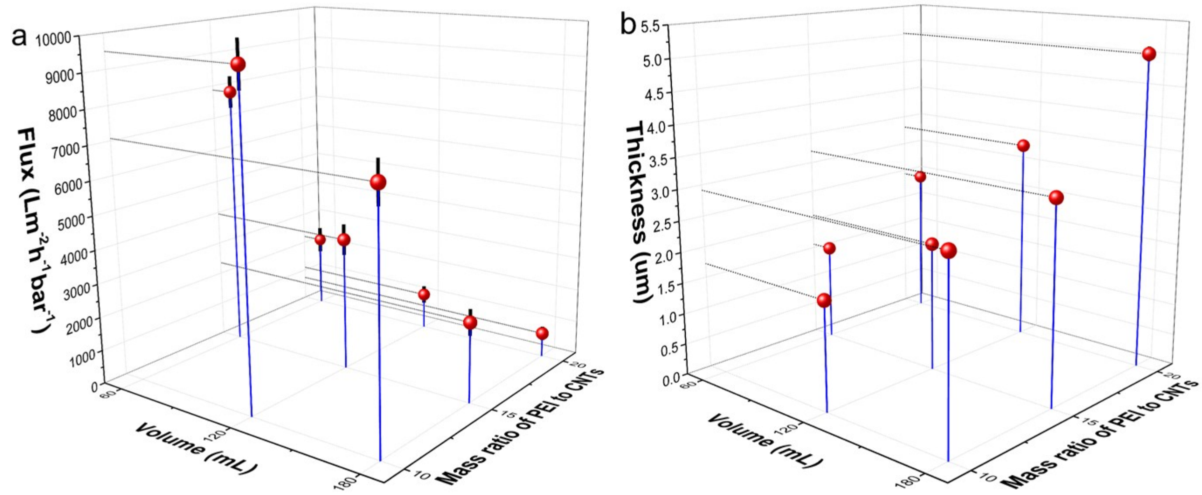

Fig. S13. (a) The thickness of the PEI@CNT nanohybrid membranes with different filtration volumes of the PEI@CNT dispersion and the mass ratio of PEI to CNTs. (b) The water permeation flux of the PEI@CNT nanohybrid membranes with different filtration volumes of the PEI@CNT dispersion and the mass ratio of PEI to CNTs.

14. The influence of pH on the water permeation flux.

The water permeation flux of $PEI_{15}@CNT_{120}$ nanohybrid membranes at the pH of 1.0, 3.0, 7.0, 11.0 and 13.0 was shown in Figure S14. And the results indicated that the membrane had stable water flux at pH range of 1.0 to 13.0.

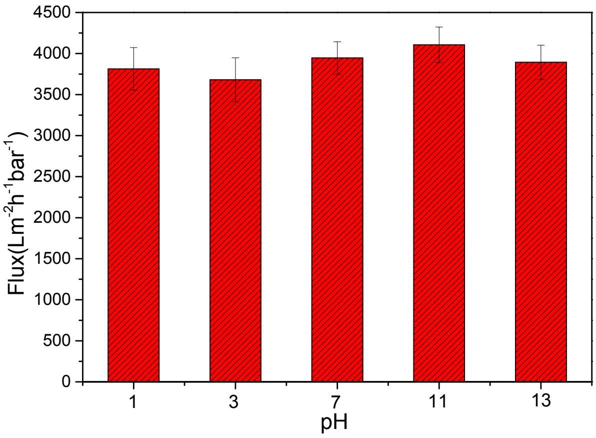

Fig. S14. The water permeation flux of PEI_{15}@CNT_{120} nanohybrid membranes at the pH of 1.0, 3.0, 7.0, 11.0 and 13.0.

15. The influence of pH on the water permeation flux.

The water permeation flux of PEI_{15}@CNT_{120}-TMC_2 nanohybrid membranes at the pH of 1.0, 3.0, 7.0, 11.0 and 13.0 was shown in Figure S15. And the results indicated that the membrane had stable water flux at pH range of 1.0 to 13.0.

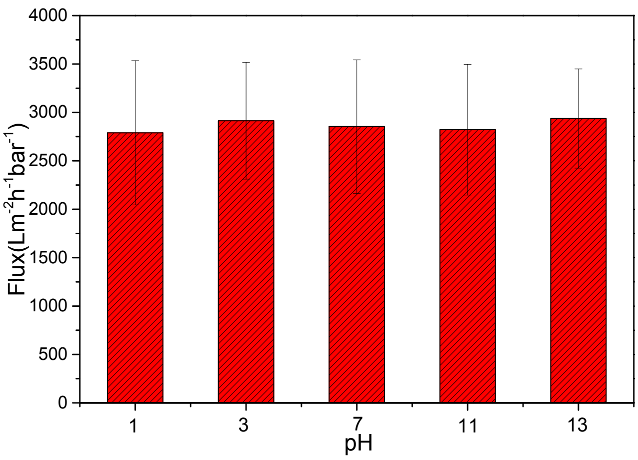

Fig. S15. The water permeation flux of PEI15@CNT120 nanohybrid membranes at the pH of 1.0, 3.0, 7.0, 11.0 and 13.0.

16. The microscopic pictures of the emulsions before and after separation

The microscope pictures of the emulsion before and after separation were shown in Fig. S16, and the results indicated that the emulsion was successfully separated in one step.

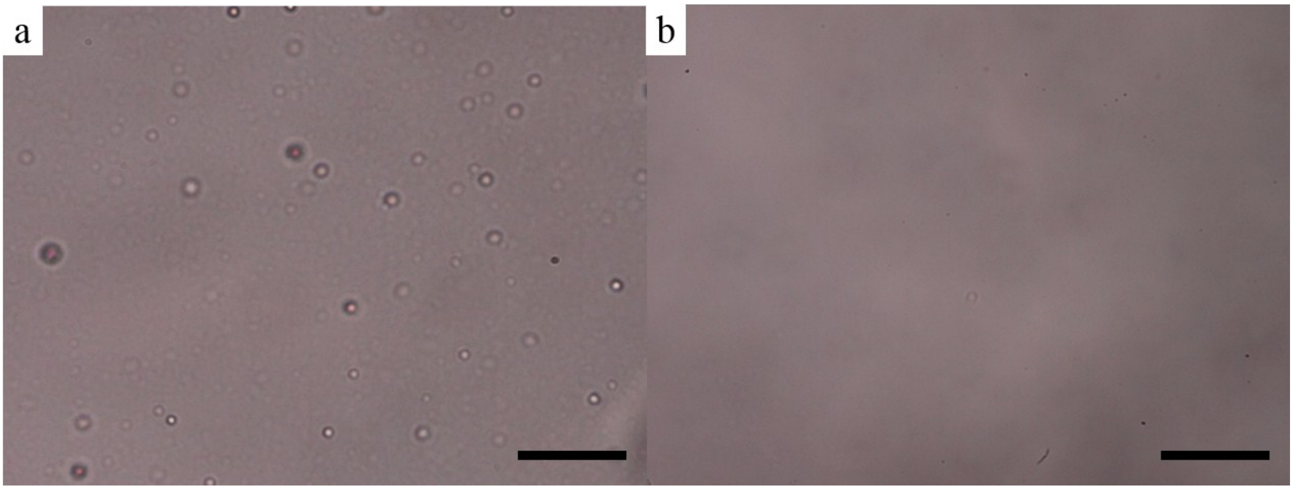

Fig. S16. The microscope pictures of the emulsion before (a) and after (b) separation, and the scale bars represented 5 μm

17. Characterization of oil-in-water emulsions

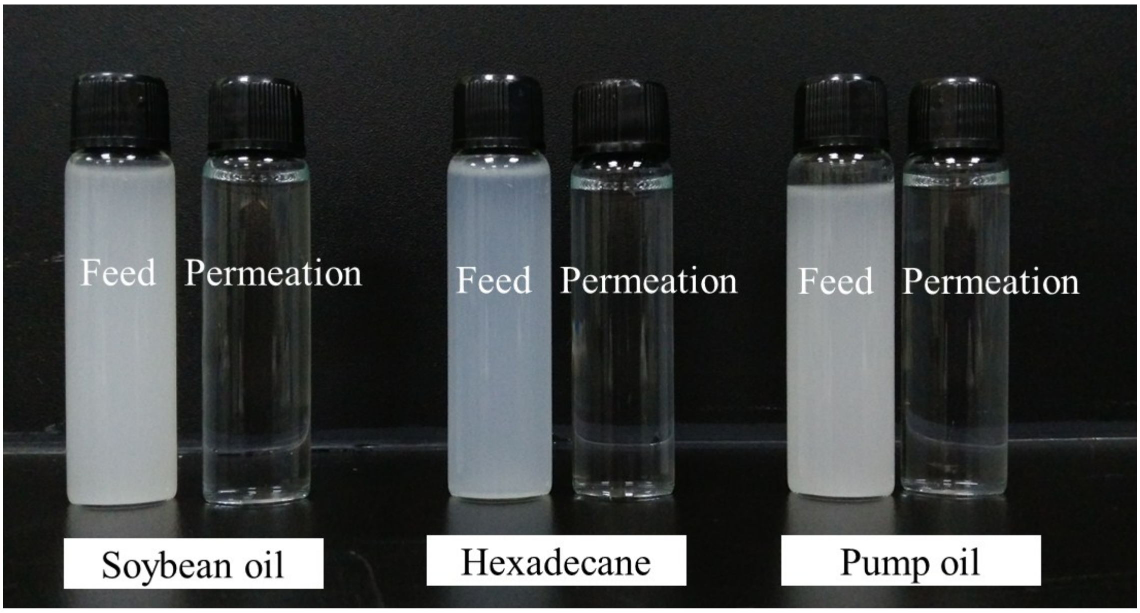

Fig. S17. Digital photos of different emulsions before and after separation including soybean oil-in-water, hexadecane-in-water and pump-in-water emulsions.